Frequency-invariant temporal ordering of interneuronal discharges during hippocampal oscillations in awake mice

Csaba Varga[a,b,1], Peyman Golshani[b,2], and Ivan Soltesz[a,2]

[a]Department of Anatomy and Neurobiology, University of California, Irvine, CA 92697; and [b]Department of Neurology, David Geffen School of Medicine, University of California, Los Angeles, CA 90095

Endogenous brain rhythms occurring at various frequencies and associated with distinct behavioral states provide multiscale temporal windows that enable cells to time their spiking activity with high precision, which is thought to be important for the coding of information in neuronal circuits. However, although the selective timing of GABAergic inputs to specific spatial domains of principal cells are known to play key roles in network oscillations, the in vivo firing patterns of distinct hippocampal interneurons in awake animals are not known. Here we used a combination of juxtacellular labeling techniques with recordings from anesthesia-free, head-fixed mice running or resting on a spherical treadmill to study the oscillation-dependent discharges by two major interneuronal subtypes, the perisomatically projecting parvalbumin-positive basket cells (PVBCs) and distal dendritically projecting oriens lacunosum molecular (OLM) cells. Recordings of the spiking activity of post hoc-identified CA1 interneurons during theta (5–10 Hz), gamma (25–90Hz), epsilon ("high-gamma"; 90–130 Hz), and ripple (130–200 Hz) oscillations revealed both cell type- and behavioral state-dependent entrainments of PVBC and OLM cell discharges in awake mice. Our results in awake mice differed in several respects from previous data on interneuronal discharge patterns in anesthetized animals. In addition, our results demonstrate a form of frequency-invariant, cell type-specific temporal ordering of inhibitory inputs in which PVBC-derived perisomatic inhibition is followed by OLM cell-generated distal dendritic inhibition during each of the network oscillation bands studied, spanning more than an order of magnitude in frequencies.

Brain state-specific network oscillations in the theta, gamma, epsilon, and ripple frequencies reflect the temporally structured, coordinated activation of principal cell populations in the hippocampus and its connected structures (1–5). These distinct oscillations with their characteristic frequency bands occur during different behaviors. Theta oscillations, which often appear with nested gamma and epsilon oscillations, are prominent during locomotion and rapid eye movement (REM) sleep, whereas ripple waves are present mostly during consummatory states, quiet wakefulness, and slow-wave sleep (6–11). The various oscillatory patterns likely serve distinct computational roles in the circuit. For example, the differential phase coupling of epsilon and gamma oscillations to theta oscillations in the CA1 has been suggested to route information selectively from the entorhinal cortex and CA3 (ref. 12, but also see refs. 13 and 14). In general, network oscillations occurring at different timescales are associated with the encoding, consolidation, and retrieval of information, and experimental perturbation of the phase-locked firing during distinct oscillations results in functional deficits (15, 16).

It has been recognized that different GABAergic cell types innervating specific postsynaptic domains release GABA at particular times during behaviorally relevant network oscillations (17), underscoring the fundamental unity of neuronal space and time as reflected in the recently coined term "chronocircuit" (18). However, a better understanding of the rules governing the

organization and functions of hippocampal chronocircuits has been hindered by the lack of data on the in vivo spike timing of anatomically and neurochemically identified interneurons during hippocampal network oscillations from awake, anesthesia-free animals. The reason for the difficulty in obtaining unambiguous data from identified interneurons in awake animals is technical in nature. Multiple single-unit recordings from freely moving animals cannot identify the recorded units definitively as belonging to particular interneuronal subtypes, because the axo-dendritic structure cannot be visualized, and the expression of defining cellular markers cannot be determined. In addition, even when multiunit recordings are combined with Cre-line–based optogenetics (19), cell identification has been limited to broad categories such as parvalbumin- or somatostatin-expressing cells (*Discussion*).

Here we report the brain state-specific discharge patterns of two major dendritically or perisomatically projecting interneuronal subtypes in the CA1 region. The results were obtained using juxtacellular recording and labeling techniques (20) in anesthesia-free, head-fixed mice that were running or resting on a spherical treadmill (21, 22), followed by post hoc identification of the recorded cells. We find that parvalbumin-positive basket cells (PVBCs) and most oriens lacunosum molecular (OLM) cells are significantly modulated by theta, gamma, epsilon, and ripple oscillations, with the degree of modulation dependent on both the cell type and the oscillatory frequency. In addition, the data indicate a consistent temporal ordering of PVBC and OLM discharges during individual oscillatory cycles regardless of the oscillatory frequency, with the firing of PVBCs preceding the discharges of OLM cells from the slowest (theta) to the fastest (ripple) oscillations. These findings provide insights into the mechanisms of generation of theta, gamma, epsilon, and ripple oscillations and indicate that delayed inhibitory input onto the distal dendrites of pyramidal cells may play a critical role for hippocampus-dependent computations across a broad range of oscillations and related brain states.

Results

The data in this paper were obtained by combining juxtacellular recording and labeling methods with the technique of head-restrained mice that can run freely or rest on a spherical treadmill. Each interneuron included in this study was recorded during theta, gamma, epsilon, and ripple oscillations (one exception was a single OLM cell for which only the theta-related firing
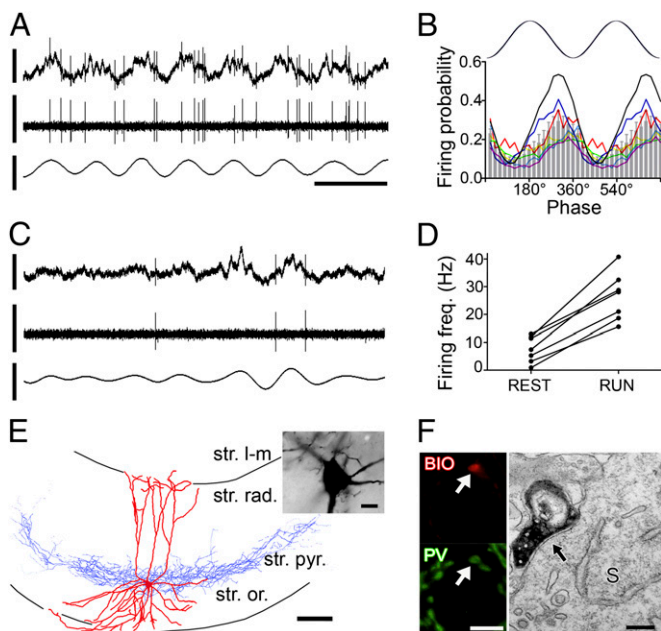
Fig. 1. Entrainment of PVBCs during theta oscillations in anesthesia-free mice. (*A*) Single-unit activity of a PVBC during running-associated theta oscillations. Filter settings for the illustrated traces: (*Top*) 0.8 Hz–5 kHz; (*Middle*) 500 Hz high-pass; (*Bottom*) theta (4–10 Hz) band pass. (*B*) Firing probability as a function of theta phase (gray bars: average; colored traces represent individual cells; color codes for individual cells within the PVBC and OLM cell classes are consistent throughout the figures; *n* = 7). The top trace is an idealized LFP theta (peaks, 180°/540°; trough, 360°/720°); note that the preferential firing (peak of gray bars) occurs before the trough. (*C*) Activity of the cell in *A* during immobility (same filters as in *A*); note the irregular firing and LFP. (*D*) Firing frequency of PVBCs during resting and running periods. All cells increased their discharge rate during running. (*E*) Camera lucida reconstruction of the biocytin-filled PVBC whose activity is shown in *A* and *C*. Axons (partially reconstructed from three 60-μm sections) are blue, and dendrites (fully reconstructed) are red. l-m, lacunosum moleculare; or, oriens; pyr, pyramidal; rad, radiatum; str. stratum. (*Inset*) Photomicrograph of the soma and the proximal dendrites of the illustrated cell after conversion of the fluorescent biocytin label to a more permanent signal with DAB. (*F*) (*Left*) parvalbumin-positive axon terminal of the PVBC shown in *E*. BIO, biocytin. (*Right*) Representative electron microscopic image shows an axon terminal of the same cell; the synaptic contact (arrow) was on a soma (S) in stratum pyramidale. (Scale bars: *A* and *C*: vertical: 0.5 mV; horizontal: 200 ms; *E*: 100 μm; *Inset* in *E*: 10 μm; *F*: light microscopy: 5 μm, electron microscopy: 0.5 μm.)

could be analyzed), and all were recovered and identified post hoc based on their axonal and dendritic arborizations and immunocytochemical characteristics.

Discharges of PVBCs and OLM Cells During Theta Oscillations in Drug-Free, Nonanesthetized Mice. We first examined the properties of perisomatically projecting PVBCs (*n* = 7) in awake, head-fixed animals (Fig. 1) during theta oscillations. The cell bodies of PVBCs were located within the stratum pyramidale or at the border of the pyramidale and oriens layers, with their axons arborizing mostly in the stratum pyramidale. [Electron microscopy in two PVBCs verified that the postsynaptic targets were, as expected, pyramidal cell somata and proximal dendrites in 25 of 27 boutons examined (Fig. 1*F*); these electron microscopic data show that the cells were not parvalbumin-positive axo-axonic (chandelier) cells that target the axon initial segment (18).] The predominantly vertically oriented dendrites of PVBCs branched in the oriens and radiatum layers, with only rare, short branches entering the lacunosum moleculare (Fig. 1*E*). The local field potentials (LFPs) recorded with a separate electrode situated in

the pyramidal cell layer 200–300 μm from the juxtacellular electrode (*Experimental Procedures*) exhibited prominent theta oscillations during periods when the mouse was running. The PVBC firing rates increased significantly, from 8.2 ± 5.6 Hz during nonrunning episodes to 25 ± 8.4 Hz during running (*n* = 7; *P* < 0.0001, paired *t* test) (Fig. 1 *A*, *C*, and *D*). In addition, the PVBCs discharged preferentially during the late descending phase of the theta waves (307 ± 22°; note that 0° and 360° correspond to the trough and 180° to the peak of the LFP) (Fig. 1*B*).

Next, we compared the spike-timing behavior of PVBCs with that of the dendritically projecting OLM interneurons (Fig. 2). The cell bodies and dendrites of OLM cells were located in the stratum oriens with axons arborizing in the stratum lacunosum moleculare, coaligned with the major termination zone for the temporoammonic fibers (*n* = 6) (Fig. 2*F*). All cells showed immunoreactivity for somatostatin and metabotropic glutamate receptor 1 alpha (mGluR1α) (Fig. 2*E*) (23); in addition, weak parvalbumin immunoreactivity was detected in one of three cells tested (17, 18). The OLM cells increased their discharge rates from 10.4 ± 5.4 Hz during nonrunning episodes to 29.8 ± 12.6 Hz during running (Fig. 2 *A*, *C*, and *D*). The peak firing probability of the cells was close to the trough of the running-associated theta oscillations (346 ± 32°; *n* = 6) (Fig. 2*B*).
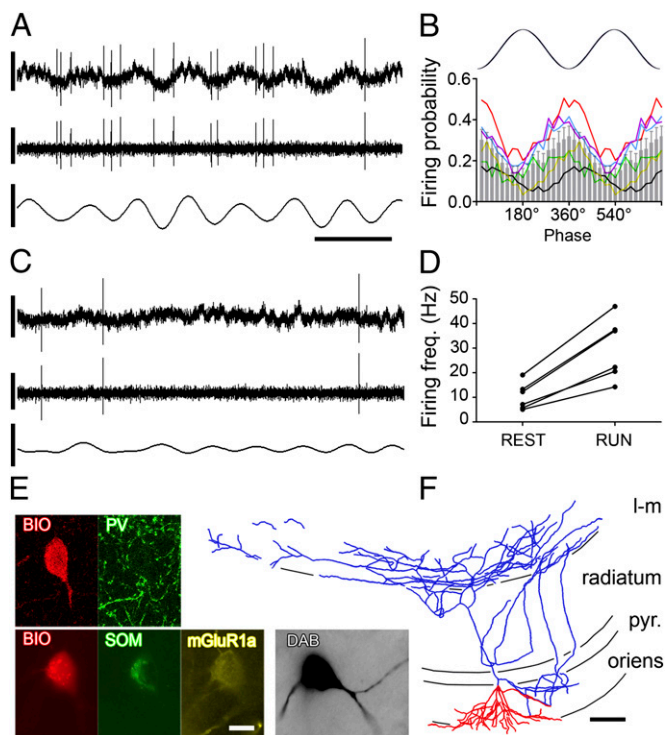

Fig. 2. Entrainment of OLM cells during theta rhythm. (*A*) Single-unit activity during running-associated theta oscillations. Filter settings for the illustrated traces are as in Fig. 1. (*B*) Firing probability as a function of theta phase (gray bars: average; colored traces represent individual cells). (*C*) Firing of the OLM cell in *A* during immobility. (*D*) Firing frequency of OLM cells during resting and running periods. (*E*) Immunopositivity of the cell shown in *A* and *C* for somatostatin and mGluR1a but not for parvalbumin. (*F*) Reconstruction of the same cell (axons: blue, partly reconstructed from five 60-μm sections; dendrites: red, complete reconstruction). (*Inset*) Photomicrograph of the soma and the proximal dendrites of the illustrated cell after conversion of the fluorescent biocytin label to a more permanent signal with DAB (image taken at a different focal plane than in *E*). (Scale bars in *A* and *C*: vertical, 0.5 mV, horizontal, 200 ms; scale bars in *E*: 10 μm; scale bars in *F*: 100 μm.)

These data show that both cell types increased their firing rates significantly during running as compared with nonrunning episodes. Surprisingly, although PVBCs generally are considered an interneuronal type that on average fires more frequently than OLM cells under all conditions, our data demonstrate that the firing rates of PVBCs and OLM cells (25 Hz and 29.8 Hz, respectively) were similar during running-associated theta rhythms. In addition, the phase-preferential firing of PVBCs and OLM cells during theta oscillations was statistically different ($P = 0.03$; Watson–Williams circular test). The difference (39°) between the theta-phase preferences indicates that, on average, the peak of the perisomatic inhibition provided by PVBCs during theta oscillations precedes the maximal inhibition of the distal apical dendrites elicited by GABA release from the OLM cells by ~11–22 ms (with theta oscillations being 5–10 Hz).

In addition, the properties of the juxtacellularly recorded single-unit spikes during running in the two cell types were compared. The data showed significant differences (Mann–Whitney tests) in spike duration (time from positive to negative peak: PVBC, 0.21 ± 0.0 ms; OLM, 0.26 ± 0.0 5 ms; $P = 0.04$) and refractory period (PVBC, 2.9 ± 1 ms; OLM, 6.1 ± 2.3 ms; $P = 0.0075$) but not in spike asymmetry (PVBC, 0.82 ± 0.06; OLM, 0.85 ± 0.09; $P = 0.57$) or bursting probability (PVBC, 0.12 ± 0.07; OLM, 0.09 ± 0.07; $P = 0.43$) (for calculations of these spike parameters, see *Experimental Procedures*). Therefore, differences in spike properties may aid in the separation of putative PVBC and OLM cell units during extracellular recordings (*Discussion*).

Entrainment of Interneurons During Gamma Oscillations. Gamma rhythms in the hippocampus can occur during wakefulness, including exploratory behavior. Gamma-frequency oscillations have been suggested to play key roles in the propagation of information across cortical areas (24–27) with the synchronous gamma-related spiking in two groups of spatially distinct neurons potentially contributing to the "binding" of information in downstream postsynaptic cell clusters (24). Although there is ongoing debate about the precise roles of gamma oscillations in specific aspects of information processing, there is broad agreement that perisomatic inhibition is important in the generation of gamma oscillations (28). However, there is no definitive evidence for the entrainment of distinct, morphologically and immunocytochemically identified interneuronal classes by gamma oscillations in nonanesthetized animals in vivo. Therefore, we next asked whether the firing of PVBCs and OLM cells is modulated significantly during gamma oscillations (18, 29). Our results showed that the discharges of all PVBCs were entrained significantly during gamma oscillations (Fig. 3). However, the power of this modulation was only moderate ($r = 0.18 ± 0.06$; $n = 7$), especially as compared with the modulation of PVBCs during epsilon and ripple oscillations (see below). The PVBCs preferentially discharged close to the midpoint of the rising phase of the gamma waves (107 ± 17°) (Fig. 3B). In contrast, although the firing of three of five OLM cells was entrained by gamma oscillations ($r = 0.12 ± 0.02$ for the significantly modulated cells) (Fig. 3 C and D), no significant modulation in firing could be observed for the other two OLM cells (modulation for all five OLM cells: $r = 0.1 ± 0.03$). The preferred phase of firing of the significantly modulated OLM cells was 143 ± 12°. Therefore, these data indicate that, although the power of gamma modulation is stronger for PVBCs than for OLM cells, the modulation is not particularly robust for either cell type (see below and also see summary data in Fig. 6, *Right*). In addition, these results show that during gamma cycles the preferred phase of discharges occur earlier on average in PVBCs than in OLM cells, a temporal ordering similar to that described above for theta waves.
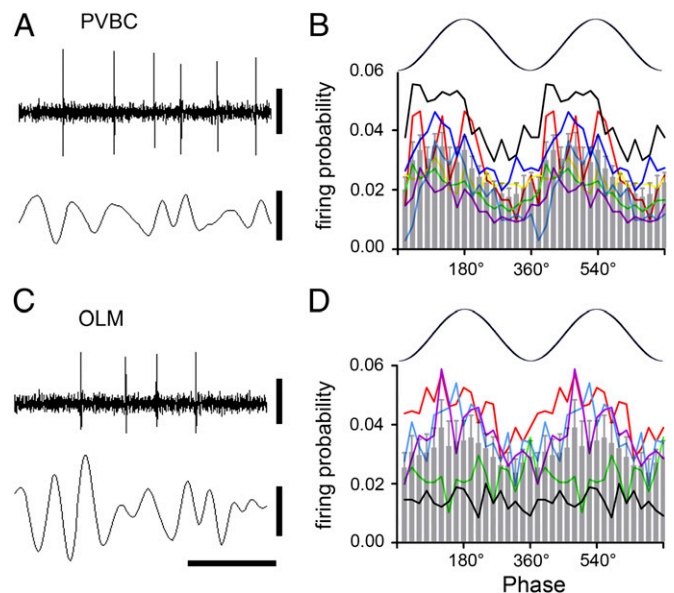

Fig. 3. Firing of identified PVBCs and OLM cells during gamma oscillations. (A and C) (*Upper*) Extracellular unit recordings during gamma oscillations and (*Lower*) LFP (25–90 Hz band pass-filtered) recordings. LFP was recorded extracellularly with a second electrode in the stratum pyramidale from an identified PVBC (A) and an OLM cell (C). (B and D) Firing probability as a function of gamma phase (gray bars: average; different colors indicate individual cells) from PVBCs (B) and OLM cells (D). Note that all PVBCs (n = 7) were phase locked close to the midpoint of the ascending phase of the gamma oscillation; two of the five OLM cells did not show phase locking, and the three OLM cells that were phase locked fired later than the PVBCs during individual gamma waves. (Scale bars in A and C: unit recordings, 0.5 mV; LFP, 0.2 mV; time scale, 50 ms.)

Modulation by Interneuron Firing in the Epsilon (High-Gamma) Range. During running, epsilon epochs (90–130 Hz) on average are nested close to the trough of the theta oscillations (7, 30), occurring close to the time of the highest discharge probability of PVBC and OLM cells (see above). Therefore, we next tested whether the discharges of PVBCs and OLM cells are entrained by and temporally aligned to particular phases of epsilon oscillations. All PVBCs were strongly phase locked to the epsilon oscillations (Fig. 4 A and B; note that the fast epsilon oscillations, similar to the gamma and ripple oscillations, were recorded with a separate, nearby LFP electrode located within the stratum pyramidale; see *Experimental Procedures*). The peak of modulation was in the early ascending phase of the epsilon waves (62 ± 19°) (Fig. 4B), with a high degree of phase locking ($r = 0.39 ± 0.08$).

The OLM cells (n = 5) were moderately but significantly entrained during epsilon oscillations ($r = 0.23 ± 0.09$) (Fig. 4 C and D). The peak of epsilon-related phase preference of OLM cell discharges was significantly delayed with respect to the phase preference of the PVBC firing (136 ± 15° vs. 62 ± 19°; $P < 0.001$; Watson–Williams test). In addition to the differences in the preferred phases of firing, the two cell groups also differed in the strength of modulation during epsilon oscillations, with the OLM cells being significantly less modulated by epsilon waves than PVBCs (0.23 ± 0.09 vs. 0.39 ± 0.08; $P = 0.03$; two-tailed Mann–Whitney test). These data show a robust modulation of PVBC firing 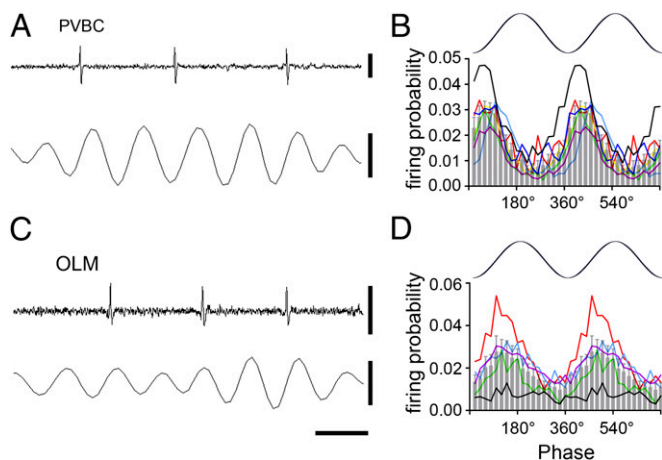and a moderate modulation of OLM cell activity by epsilon waves, and, similar to findings for theta and gamma rhythms, PVBC firing precedes the OLM cell discharges during epsilon oscillations.

Fig. 4. Phase locking of PVBCs and OLM cells to epsilon oscillations. (*A* and *C*) (*Upper*) Extracellular unit recordings during epsilon oscillations. (*Lower*) LFP trace (90–130 Hz band-pass filtered) recorded with a separate electrode in the stratum pyramidale from a PVBC (*A*) and an OLM cell (*C*). (*B* and *D*) Firing probability as a function of epsilon phase (gray bars: average; different colors indicate individual cells) from PVBCs (*B*) and OLM cells (*D*). Note that the PVBCs preferentially fire during the early ascending phase, whereas OLM cells fire during the late ascending phase of the epsilon waves. (Scale bars in *A* and *C*: unit recordings, 1 mV; LFP, 0.2 mV; time scale, 10 ms.)

Differential Firing of PVBCs and OLM Cells During Ripple Oscillations.
In contrast to theta oscillations that typically are present during exploration and REM sleep, sharp-wave ripples occur during immobility, consummatory behaviors, and slow-wave sleep (1). Sharp-wave ripples in the CA1 are generated by transient population bursts in the CA3 network and are expressed as sharp waves in the dendritic layers and fast (130–200 Hz) ripple oscillations in the somatic layer (1, 31). Although perisomatic inhibition is thought to play a key role in the generation of ripples (32, 33), the entrainment of specific interneuronal subtypes by ripple oscillations under anesthesia-free conditions is not known. Therefore, we examined the firing of identified interneurons during ripple oscillations occurring during nonrunning periods.

PVBCs ($n = 7$) discharged robustly during ripple oscillations, with their firing rates increasing from 8.2 ± 5.6 Hz to 75 ± 17 Hz during ripple episodes (Fig. 4 *A* and *B*). In addition, the discharges of PVBCs showed strong phase locking ($r = 0.58 \pm 0.1$) to the early ascending phase of the ripple waves ($40 \pm 16°$) (Fig. 5*E*). In contrast, the OLM cells ($n = 5$) had a generally lower firing probability during ripples (Fig. 5 *A–D*). However, the mean firing rate of OLM cells also increased during ripples, from 10.4 ± 5.4 Hz during interripple nonrunning periods to 25.4 ± 7 Hz during the ripples. When the cells were analyzed individually, four OLM cells showed a significant increase in firing probability during the ripple periods [$P < 0.001$; note that, in the case of the one cell that did not show significant increase in firing during ripples, a relatively low number ($n = 25$) of ripples were detected during the recording]. OLM cell firing occurred on a lower proportion of the ripples ($46 \pm 13.8\%$) than PVBC firing ($98.5 \pm 2.2\%$) ($P = 0.0054$, Mann–Whitney test) (Fig. 5 *A–D*). In addition, PVBCs exhibited a high discharge probability from the beginning of the ripple oscillations, whereas the increase in OLM cell firing occurred in a more delayed fashion (Fig. 5*C*). Interestingly, although the firing of OLM cells during ripples was relatively weaker and more delayed than the firing of PVBCs, the spikes in OLM cells also were robustly phase locked ($r = 0.61 \pm 0.14$; $n = 5$) to the ripple waves. The preferential firing in OLM cells occurred during the late ascending phase of the ripple waves ($141 \pm 13°$) (Fig. 5*E*), significantly later than that of the

PVBCs ($P < 0.001$; Watson–Williams test). These results demonstrate distinct discharge patterns of PVBCs and OLM cells during ripple oscillations in the awake, nonanesthetized animal. Specifically, PVBCs fire relatively early and during most ripple episodes, whereas OLM cells discharge later and during only about half of the ripple episodes. Interestingly, although the firing frequencies of OLM cells during theta and ripple oscillations were comparable (29.8 Hz and 25.4 Hz, respectively), the firing of PVBCs was three times more frequent during ripples than during theta oscillations (25 Hz vs. 75 Hz). Despite the differences in firing rates between the two cell types, the phase locking of spikes to ripple waves is of comparable magnitude in PVBCs and OLM cells. In addition, during individual ripple waves the phase-preferential firing of PVBCs occurs earlier than that of OLM cells, similar to observations during the other, slower network oscillations.

Discussion

Juxtacellular Recordings of Interneurons in the Hippocampus of Awake Mice.
In this study, juxtacellular single-cell recording and labeling techniques were used in head-fixed, awake mice to reveal the in vivo action potential firing patterns of two major hippocampal GABAergic interneuronal subtypes without the influence of anesthetic drugs. PVBCs are one of the two key, nonoverlapping basket cell classes (34, 35) innervating the perisomatic region of principal cells, whereas CA1 OLM cells provide a major source of distal dendritic inhibition in the lacunosum moleculare layer that receives temporoammonic inputs from the entorhinal cortex. Because of the predicted importance of PVBCs and OLM cells in regulating hippocampal network activity, these two major interneuronal subtypes have been studied extensively both in vitro and in vivo. PVBCs in the CA1 region have been shown to receive substantial excitatory input from both CA3 and local CA1 pyramidal cells, with the CA1 input exhibiting short-term depression upon repeated stimulation (36, 37). PVBCs fire fast, nonaccommodating action potentials and have fast membrane time constants, and GABA-release from their axon terminals takes place in a synchronous manner with tight temporal association between the presynaptic action potential and the postsynaptic response (38, 39). OLM cells receive their primary, markedly facilitating excitatory inputs from local CA1 pyramidal cells with minimal input from CA3 pyramidal cell axon collaterals (40, 41), and their intrinsic biophysical properties are thought to enable them to participate preferentially in theta-frequency activity (42–46). Therefore, by focusing on PVBCs and OLM cells, the present study aimed to determine the temporal structure of spiking activity of two key sources of perisomatic and distal dendritic GABAergic input to CA1 pyramidal cells under anesthesia-free conditions and across a range of network oscillatory frequencies spanning a wide range from <10 Hz to >100 Hz, with four specific frequency bands associated with distinct behavioral states and functions.

The current methodology involving juxtacellular recording from head-fixed, drug-free animals followed by unambiguous morphological and immunocytochemical identification of every cell, is of relatively low yield and labor intensive. However, it is important to emphasize that rigorous identification of interneurons in general cannot be done without the visualization of the axonal morphology (because the axonal morphology determines where GABA is released along the somatodendritic axis of principal cells from any given interneuron) and the characterization of the expression of key immunocytochemical markers (to differentiate between cells with similar axonal target-specificity). For example, axonal morphology alone is not sufficient to differentiate PVBCs and cholecystokinin-positive basket cells, and in ambiguous cases electron microscopic analysis of the postsynaptic targets may be necessary to distinguish PVBCs from axo-axonic (chandelier) cells, both of which express parvalbumin
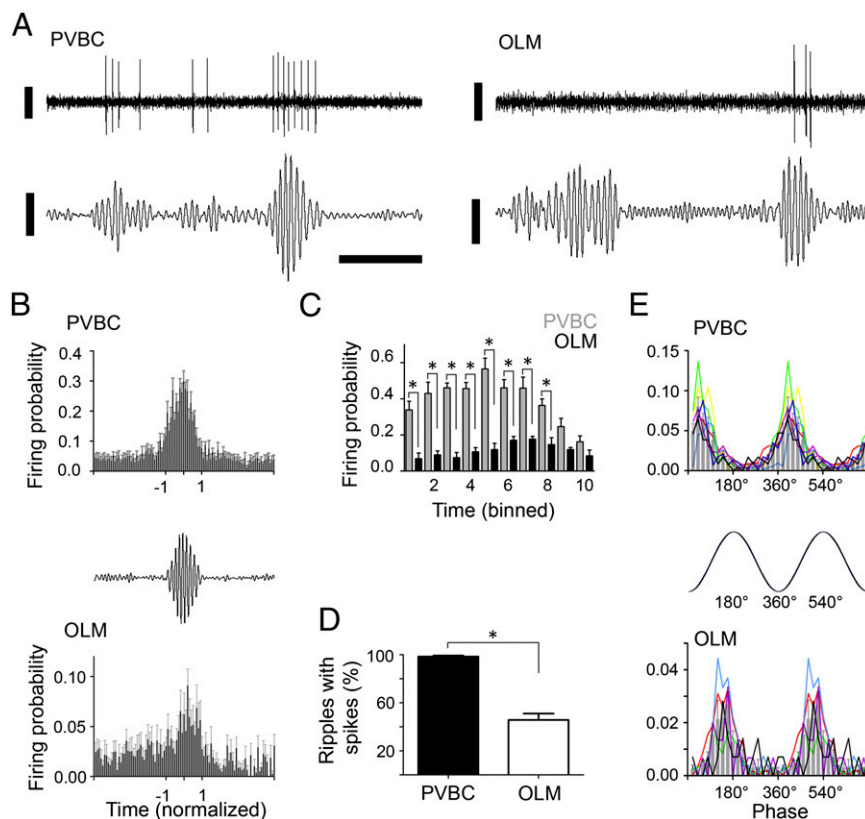
Varga et al.

Fig. 5. Interneuronal spiking during ripple oscillations in the awake mouse. (*A*) Unit recordings (*Upper*) during ripple oscillations (*Lower*) from a PVBC (*Left*) and an OLM cell (*Right*). (*B*) Firing probability as a function of normalized time (start of ripple: −1; end of ripple: +1) for PVBCs (*Upper*) and OLM cells (*Lower*). (*C*) Cell type-specific temporal evolution of firing probability during ripples. *$P < 0.05$; Bonferroni's multiple comparisons test. (*D*) Percent of ripples during which PVBCs or OLM cells fired at least one spike. Note that PVCBs fired during most ripples, whereas OLM cells fired during about half of the ripples. *$P < 0.05$; Bonferroni's multiple comparisons test. (*E*) Firing probability as a function of the phase of the ripple wave (gray bars: average; different colors indicate individual cells) from PVBCs (*Upper*) and OLM cells (*Lower*). (Scale bars: unit recordings, 0.5 mV; LFPs, 0.2 mV; time scale, 100 ms.)

and have axons largely restricted to the CA1 pyramidal cell layer. Extracellularly recorded action potential characteristics (as can be obtained from tetrode recordings) likewise are insufficient for unambiguous classification, because several distinct GABAergic subtypes have similar spike properties; for example, PVBCs, axo-axonic cells, and bistratified cells are all fast-spiking interneurons. Currently, optogenetic approaches to cell-type identification based on the cre system (19, 47) also are limited to broadly defined cell groups, e.g., parvalbumin- or somatostatin-expressing cells. For example, parvalbumin is expressed by axon initial segment-targeting axo-axonic cells, somatically and proximal dendritically projecting PVBCs, dendrite-innervating bistratified cells, and some OLM cells; similarly, somatostatin is expressed by OLM cells, bistratified cells, and long-range projecting interneurons (18). It is interesting that identified somatostatin-positive OLM cells in our study fire at the trough of the theta rhythm, whereas the optogenetically identified somatostatin-positive cells show a firing range spanning from the trough to the late rising phase of the theta oscillations (19).

The ability to record from post hoc-identified interneurons in drug-free, awake animals adds further insights to the data obtained from anesthetized preparations. In addition to the lack of general anesthetic drugs, many of which modulate the GABAergic system and thus interfere with the temporal and spatial coordination of interneuronal networks, the combination of juxtacellular recordings and the head-fixed mouse on a spherical treadmill model made it possible for us to study interneuronal spiking activity during both low- and high-frequency oscillations in detail, which is difficult to achieve under anes-

thesia (31). Indeed, urethane anesthesia (a general anesthetic often used in the in vivo studies focused on interneurons) has been shown to have effects on CA1 network oscillations that are similar to those observed following the removal of the entorhinal cortex (31), making it challenging to determine interneuronal discharge characteristics during rhythms that are modulated by temporoammonic inputs (e.g., epsilon oscillations) (7). Given the influence of anesthesia on neuronal networks, it is not surprising that our data revealed some differences in PVBC and OLM cell characteristics in awake vs. anesthetized preparations. In particular, the preferential discharge of PVBCs under anesthesia was reported to be at the midpoint (271°) of the descending phase of the theta rhythm (17), whereas PVBCs under our drug-free conditions fired 36° later, during the late falling phase of the theta cycle. Similarly, most OLM cells showed no gamma modulation under anesthesia (48), whereas a majority of OLM cells under awake conditions (albeit not all) were significantly gamma modulated. In addition, OLM cells were shown to decrease their firing rates during ripple episodes under anesthesia (13), whereas OLM cells in our recordings from awake animals increased (or, in the case of one cell, did not change) their firing rates during ripples. However, it should be noted that, in addition to anesthesia, potential species-specific effects (rat vs. mouse) might have contributed to the differences between previous reports (17, 48) and the present data on the network oscillation-related spiking activities of PVBCs and OLM cells in vivo.

Temporal Differences Between PVBC and OLM Cell Discharges During Hippocampal Network Oscillations in Awake Mice. A major finding that emerged unexpectedly from the current investigation was the temporal ordering of PVBC and OLM cell firing across a wide range of oscillatory frequencies. It is interesting to compare the differences between the preferred phases of discharges by PVBCs and OLM cells: 39° for theta, 36° for gamma, 74° for epsilon; and 101° for ripples. Therefore, as the frequency of gamma, epsilon, and ripple oscillations increases, there is a corresponding increase in the difference in the preferred firing phases of PVBCs and OLM cells, resulting in an absolute time difference between the firing of these two cell classes that stays remarkably constant (ranges are calculated according to the lower and upper limits of the oscillatory bands: 1.1–4 ms for gamma; 1.6–2.2 ms for epsilon; and 1.4–2.2 ms for ripples). Therefore, for the faster (gamma, epsilon, and ripple) oscillations, the lower limits of the differences between the PVBC and OLM cell discharges correspond approximately to a single synaptic delay. Thus, regardless of the frequency above 25 Hz, the key determinant of the temporal ordering of firing of PVBCs and OLM cells appears to be an extra synaptic step necessary for the excitation of OLM cells. It seems reasonable to assume that the latter, additional synaptic step may be caused by OLM cells being driven primarily by facilitating excitation from CA1 pyramidal cells (36, 49), whereas PVBCs receive initially strong but depressing inputs from local CA1 pyramidal cells in addition to being driven by excitatory inputs from Schaffer collaterals. Furthermore, the frequency-invariant temporal ordering of the preferred phases of firing during the gamma, epsilon, and ripple oscillations likely is influenced also by differences in intrinsic membrane properties of the interneurons (50). In addition to membrane time constants and spike thresholds, distinct dendritic ion-channel compositions of the two cell types (45, 51, 52) likely contribute to the sequential activation. The high dendritic Kv3 expression in PVBCs, in particular, allows precise firing in response to rapid membrane potential fluctuations (51), whereas action potential initiation in dendrites of OLM cells (53) may contribute to delayed spiking during network oscillations. In addition, because inhibitory connections between interneurons are known to be important for the generation of rhythms at all frequencies (54–56), potential differences between the GABAergic inhibitory inputs to PVBCs and OLM cells also likely shape the preferential time of firing of these two interneuronal subtypes. Finally, it is interesting that the rank order of the strength of modulation of interneuronal firing during the faster rhythms was remarkably similar for PVBCs and OLM cells, with the strength of modulation increasing with the oscillation frequency for both cells (strength of modulation in ascending order: gamma, epsilon, ripple) (Fig. 6). The gamma rhythm exhibits robust cycle-to-cycle changes in amplitude and cycle duration, reflecting the fluctuations in the levels of local excitation and feed-back inhibition in the network (27). Different local assemblies of neurons are thought to be activated during successive gamma cycles (28), possibly explaining the relatively moderately entrained firing of individual interneurons during ongoing gamma oscillations in vivo. On the other hand, the strong modulation of PVBC and OLM cell firing during ripples suggests that these interneurons are recruited powerfully during ripple oscillations, when the largest proportion of hippocampal neurons fire together (14, 31, 32).

In contrast to the faster rhythms (>25 Hz), in which the difference between the preferential discharges of PVBCs and OLM cells is in the range of one or two synaptic delay(s), the temporal difference between the discharges of these two interneuronal subgroups during theta oscillations is considerably longer, in the range of 11–22 ms [estimated from the observed difference between the mean preferred phases of firing of the two cell types during theta oscillations (39°) (*Results*) and the theta frequency range of 5–10 Hz]. Such long delays seem unlikely to be
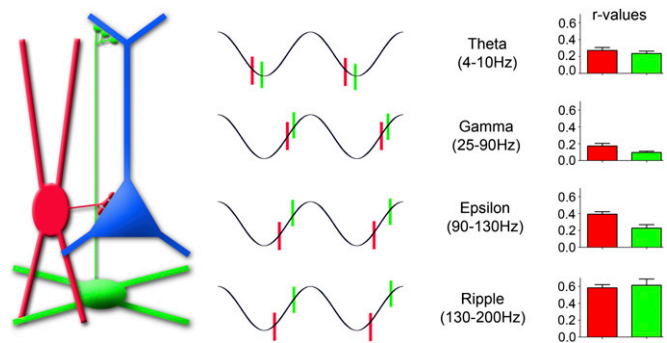

Fig. 6. Summary illustration of the oscillation frequency-independent sequential GABAergic inputs to the perisomatic region and distal apical dendrites of CA1 pyramidal cells delivered by PVBCs and OLM cells. (*Left*) A pyramidal cell (blue); PVBC (red); and OLM cell (green). (*Center*) Summary of the mean preferential phase locking of PVBCs (red) and OLM cells (green) to theta, gamma, epsilon, and ripple oscillations. (*Right*) Magnitude of phase locking of PVBCs and OLM cells. Note that for both cell types the strongest phase locking occurred during ripples, and the weakest occurred during gamma oscillations.

explained mechanistically by differential local circuit organization, differences in short-term plasticity properties, or differences in intrinsic membrane excitability alone, but a combination of these factors may be sufficient.

Finally, although our data demonstrate that it is statistically likely that a PVBC will fire before an OLM cell regardless of the frequency of the network oscillation, both cell types have a nonzero probability of firing even at the least-preferred phases in all four oscillatory bands (see Figs. 1*B*, 2*B*, 3 *B* and *D*, 4 *B* and *D*, and 5*E*). Thus sometimes the cells may spike in the reverse order (for example, based on the data in Fig. 5*E*, the probability of an OLM cell firing before a PVBC during a ripple wave is 2%). On the other hand, the variability in interneuronal spike timing may be counterbalanced by the fact that several PVBCs and OLM cells converge on a single CA1 pyramidal cell, increasing the likelihood that the bulk of the inhibitory inputs from the presynaptic PVBC and OLM cell populations arrives at the postsynaptic pyramidal cells in the expected order, i.e., PVBC inputs followed by OLM cell inputs. In this regard it is interesting that, although individual cells showed different depth of modulation during network oscillations (Fig. 1*B*), there was no consistency in the relative depth of modulation at different oscillatory frequencies for individual cells; for example, the PVBC indicated by the black trace in Fig. 1*B* had the highest *r* value for modulation relative to other PVBCs during theta, but its *r* value was among the lowest during ripples (Fig. 5*E*; the color codes for individual cells within the PVBC and OLM cell classes are used consistently throughout the figures).

Future Directions and Outlook. The precise roles and relative importance of the circuit- and intrinsic property-based mechanisms giving rise to the frequency-independent temporal ordering of PVBC and OLM cell firing during different oscillations will need to be tested in future experimental and computational investigations. Future studies also will be needed to determine the precise functional significance of the delay in firing of OLM cells relative to PVBCs during network oscillations, including the optimization of the timing of dendritic inhibition (57) to coincide with the arrival of synaptic input from entorhinal cortex and back-propagating spikes to the distal dendrites of CA1 pyramidal cells. The present results, together with future similar studies on other interneuronal types, will increase our understanding of the functional organization of hippocampal chronocircuits, which, in turn, may provide insights into their dysfunctions in psychiatric

Varga et al.

and neurological disorders. In addition, our data also will assist researchers in developing reliable, objective, quantitative criteria to achieve the long-sought goal of classifying extracellularly recorded units during behavioral experiments into specific GABAergic cell classes (58). Based on our results, extracellularly recorded putative PVBC and OLM cell units may be differentiated from each other best based on specific spike attributes (PVBCs fire faster spikes with a shorter refractory period) and ripple-related spiking properties (PVBCs fire at least once during every ripple oscillation, with distinct temporal dynamics, frequency, and preferred phase of firing). Future experiments will need to establish the degree to which these single spike- and ripple oscillation-related properties can be used to differentiate PVBCs and OLM cells from other interneuronal subtypes (e.g., PVBCs from the other fast-spiking cell classes) during extracellular recordings in awake animals.

Experimental Procedures

All experiments were approved by the Institutional Animal Care and Use Committees of the University of California at Irvine and the University of California at Los Angeles.

Head Bar Implant Surgery. Adult (2- to 3-mo-old) male and female C57BL/6 mice were anesthetized with isoflurane (induction, 4–5%; maintenance, 1–1.5%). A small portion of the scalp (infiltrated with bupivacaine, 0.5%) and fascia overlying the skull were removed, and the skull was covered with a thin layer of cyanoacrylate glue. A chronic stainless steel head-plate (adapted from ref. 59) was implanted onto the skull [centered at −2 mm anteroposterior (AP) and 2 mm lateral from midline] using dental cement. Carprofen (5 mg/kg) or flunixin meglumine (2 mg/kg) was administered as systemic analgesia.

Acclimation. The spherical treadmill consisted of an 8-inch closed-cell Styrofoam ball (Plasteel Corporation) held afloat in a stainless steel bowl (McMaster Carr) by jets of compressed air through eight inlets (adapted from ref. 21). Two to three days after the implantation, the mouse was handled extensively by the experimenter and then was placed on top of the spherical treadmill. The mouse was allowed to move freely on the ball while the experimenter rotated the ball to keep the animal on the top. The next day the animal again was acclimated to the spherical treadmill, but this time it was head-fixed by attaching the head-plate to a rigid crossbar. The animal ran or rested on the treadmill for 10–30 min. After successful acclimation to the apparatus, mice ran, groomed, and rested on the treadmill without difficulty, at which point they were prepared for juxtacellular recording.

Craniotomy Surgery. Mice were anesthetized with isoflurane, and a 1-mm craniotomy was performed at −2 mm AP and 2 mm lateral from midline. Mice were moved to the treadmill and allowed to recover from anesthesia head-fixed for at least 1 h before start of the recordings. One hour after recovering from anesthesia, the mice were alert and running or resting on the treadmill, without showing any signs of sedation. During periods of rest, mice constantly adjusted their posture, had their eyes open, and occasionally groomed.

Electrophysiology. Borosilicate glass long-tapered microelectrodes (Sutter Instruments) were pulled with a Sutter micropipette puller (P-1000). Two microelectrodes (an LFP electrode and a juxtacellular recording electrode) were lowered into the dorsal hippocampus at 15° from the vertical in the mediolateral direction so that the tips were less than 300 μm apart when they reached the stratum pyramidale. Recordings were performed using an Axoclamp 2A (Axon Instruments) or ELC-03XS universal amplifier (NPI Electronics). Field potential recordings were performed using an A-M Systems Model 3000 or a Neurodata IR283 (Cygnus Technology) amplifier. The field electrode was loaded with 0.5 M NaCl solution and placed within or close to the stratum pyramidale, identified as the location where the largest amplitude sharp wave-associated ripple oscillations could be recorded. The other microelectrode [12–20 MΩ, 0.5 M NaCl, 1.5–2% (wt/wt) Neurobiotin] was used to perform juxtacellular recordings and subsequent labeling of the recorded neurons (17, 20). The movements of the animals during the recording sessions were videorecorded and synchronized to electrophysiological recordings. Both channels were low-pass filtered at 5 kHz and digitized at 12 or 20 kHz using NIDAQ data acquisition cards (National Instruments) and WinEDR software (Strathclyde), enabling us to monitor

spikes with both channels. Importantly, the single units recorded with the juxtacellular electrode were not observed in the LFP channel; therefore, the LFP signal was not contaminated by the spikes of the recorded interneuron. [Contamination is an important issue at higher-frequency oscillations, where the spike duration and the cycle time of the oscillation (e.g., 5–7 ms for ripples) are within the same magnitude; in contrast, contamination is not a problem in the case of the relatively slow theta oscillations.] After 10–30 min of recording, the juxtacellular electrode was advanced toward the cell, and positive 200-ms-long current pulses (1–5 nA) were applied so that the cell fired trains of action potentials for 5–10 min (17, 20). Only one interneuron per brain was labeled.

Analysis. Data were analyzed using custom-written routines in MATLAB using the Signal Processing Toolbox. Traces were zero-phase filtered using finite impulse–response filters. The juxtacellularly recorded signal was high-pass filtered at 400 Hz, and spikes were detected after crossing a threshold manually set by the experimenter (typically between 200 and 400 μV). Superimposing all detected spikes revealed single units in all cases. The LFP was band-pass filtered at theta (5–10 Hz), gamma (25–90 Hz), high-gamma (90–130 Hz), and ripple (130–200 Hz) frequencies. Theta oscillations were detected in the signal from the juxtacellular recording electrode, located in either the stratum oriens or pyramidale. For all other oscillations (gamma, epsilon, and ripple), analysis of the LFP was performed on data collected from the LFP electrode located in stratum pyramidale. Recordings were separated into distinct behavioral states, i.e., periods of running with prominent theta oscillations and periods of immobile wakefulness with sharp-wave ripples and low theta power, that were analyzed separately.

The troughs of each theta, gamma, or ripple oscillation were detected and assigned a value of 0° or 360°. The theoretical limitation of trough detection (as calculated from the sampling rate) was <0.2, 1.5, 3, and 4° for theta, gamma, epsilon, and ripple oscillations, respectively. Phase locking of spikes with the band pass-filtered LFP signal was assessed for all theta cycles during running. For gamma and epsilon oscillations, only cycles with a trough-to-peak amplitude greater than the mean amplitude of the gamma- or epsilon-filtered signal for the duration of the recording were selected for analysis (48).

Ripple detection was carried out during nonrunning periods. First, envelope detection was performed on the absolute value of the ripple-filtered signal. All local peaks of the absolute value of the ripple filter output were determined, and then cubic spline interpolation was applied to obtain the envelope. The instances in which the peaks of the envelope exceeded the threshold (7 SD of the ripple-filtered signal) were considered ripple events. The end points were obtained by determining where the envelope crossed the second threshold (2 SD of the signal). All ripple events were inspected manually, and artifacts were discarded.

The location of each spike within each theta, gamma, epsilon, and ripple cycle was determined and for each oscillation type was assigned to a phase between 0° and 360°. To represent the data in figures, the spikes were binned (size of bins = 20°). To determine whether a cell was modulated significantly during theta, gamma, epsilon, or ripple episodes, uniformity was statistically assessed with a Rayleigh test with a significance level of $P < 0.05$ (60). To quantify the depth of modulation, we summed all spike-time phases as unity vectors and normalized this sum by the number of spikes. Depending on the orientations of the different phase angles, the length of the normalized vector (r) ranged from 0 (no phase preference) to 1 (all phase angles identical). This length of the vector was used to measure the magnitude of phase modulation. The direction of r indicated the mean phase angle of the cell. The differences between phase locking of the PVBC and OLM cell populations during theta, gamma, epsilon, and ripple oscillations were quantified using the Watson–Williams circular test (29, 61). To calculate the normalized probability of spike firing during each ripple relating to the data summarized in Fig. 5B, we first binned the time period from the start to the peak of the ripple and from the peak to the end of ripple into 10 bins each and determined the number of spikes occurring in each bin. With this method (adopted from ref. 17), the ascending and descending phases of the ripples (before and after the peak) were normalized to the same length to eliminate potential asymmetries in the ripples. Normalized discharge frequencies before, during, and after the ripples were calculated. For the analysis of the ripple-related firing illustrated in Fig. 5C, individual ripples were divided into 10 bins, and the spikes were counted and summed for each bin.

To test whether action potential firing during ripples arose by chance, we used two different statistical simulations. First, the locations of all recorded spikes were pseudorandomly redistributed 1,000 times, and the number of spikes falling within ripples was calculated for each simulation. These

www.manaraa.com

numbers were sorted from highest to lowest. The P value was calculated by determining where the number of spikes occurring during ripples in the actual recordings ranked within the sorted simulated spike numbers. Ripple modulation was considered significant if the number of spikes occurring during ripples was higher than the highest 95% of the simulation results. Second, we performed another set of simulations which preserved the temporal structure of the spike trains; instead of randomizing the spike train, we circularly shifted the LFP trace by a random interval of time 1,000 times, so that the relative timing between the ripple episodes was preserved but the timing of spikes relative to the ripples was shifted. Then we again determined the number of spikes that fell within the relocated ripple events. Again, ripple modulation was considered significant if the number of spikes occurring during simulated ripples was higher than the highest 95% of the simulation results.

For analysis of single-spike properties, we followed previously described methods (19, 62). Single-spike attributes were measured during running periods. Duration of the juxtacellularly recorded spikes was measured from positive to negative peak (62). Spike asymmetry = $(a - b)/(a + b)$, where a is the positive peak of the spike and b is the smaller, second positive peak at the end of the spike (see supplementary figure 7A in ref. 19). Bursts were defined as spikes with interspike intervals <9 ms (as in ref. 19), and the number of bursts (N_B) and the number of single spikes (N_S) occurring during the analyzed period was counted for each cell; burst probability = $N_B/(N_B + N_S)$ (19).

Circular means and circular SDs were calculated using routines provided by the Circular Statistics Toolbox (63). All data are presented as mean $\pm$ SD.

Immunohistochemistry, Cell Reconstruction and Electron Microscopy. Two to four hours after the recorded cell was labeled, mice were deeply anesthetized with Nembutal and transcardially perfused with saline followed by fixative containing 4% paraformaldehyde, 0.05% glutaraldehyde, and 0.2% picric acid dissolved in 0.1 M phosphate buffer (PB) (pH = 7.4). After overnight fixation, the brains were sectioned at 60-μm thickness using a Vibratome

(Leica). All sections were first incubated in Alexa 594-conjugated streptavidin (1:1,000) (Molecular Probes), and individual sections containing the somata/dendrites/axons of the labeled cells were selected for further immunohistochemical analysis. Primary antibody mixtures were made by combining two of the following antibodies: rat anti-somatostatin (1:1,000) (MAB354; Millipore), goat anti- mGluR1α (1:1,000) (Af1220; Frontier Institute), or rabbit anti-parvalbumin (1:5,000) (PV25; Swant). The primary antibodies were visualized by DyLight 488- or DyLight 649-conjugated affinity-purified secondary antibodies raised in donkey against rat/goat/rabbit (1:1,000) (Jackson ImmunoResearch Laboratories). All antibodies were diluted in 0.1 M PB (pH 7.4) containing 0.3% Triton X-100. The slices were incubated in the primary and secondary antibody mixtures overnight and for 4 h, respectively, at room temperature. The sections then were mounted in Vectashield (Vector Laboratories), analyzed, and documented with a CCD camera attached to a conventional epifluorescence microscope (Zeiss Axioskop). Additional images were taken with an Olympus FV1000 confocal microscope (objective: PlanApoN 60×/1.42). Brightness/contrast adjustments were performed on the entire image using Adobe Photoshop CS2 program. Finally, the Neurobiotin-labeled cells were visualized with 3,3′-diaminobenzidine tetrahydrochloride (DAB; 0.015%) using a standard ABC kit (Vector). The sections then either were dehydrated and mounted or were embedded for electron microscopy (17). Dendritic and axonal arborizations were reconstructed using a drawing tube. After reconstruction, the target specificity of two of seven PVBCs was verified on serial ultrathin (70-nm) sections analyzed using a Jeol transmission electron microscope (JEM-1400), and pictures were taken with a Gatan SC1000 ORIUS CCD camera.

1. Vanderwolf CH (1969) Hippocampal electrical activity and voluntary movement in the rat. *Electroencephalogr Clin Neurophysiol* 26:407–418.
2. Buzsáki G, Leung LW, Vanderwolf CH (1983) Cellular bases of hippocampal EEG in the behaving rat. *Brain Res* 287:139–171.
3. Cohen NJ, Eichenbaum H (1991) The theory that wouldn't die: A critical look at the spatial mapping theory of hippocampal function. *Hippocampus* 1:265–268.
4. Csicsvari J, Hirase H, Czurkó A, Mamiya A, Buzsáki G (1999) Oscillatory coupling of hippocampal pyramidal cells and interneurons in the behaving Rat. *J Neurosci* 19:274–287.
5. McNaughton N, Ruan M, Woodnorth MA (2006) Restoring theta-like rhythmicity in rats restores initial learning in the Morris water maze. *Hippocampus* 16:1102–1110.
6. Buzsáki G, Chrobak JJ (1995) Temporal structure in spatially organized neuronal ensembles: A role for interneuronal networks. *Curr Opin Neurobiol* 5:504–510.
7. Colgin LL, Moser EI (2010) Gamma oscillations in the hippocampus. *Physiology (Bethesda)* 25:319–329.
8. Lubenov EV, Siapas AG (2009) Hippocampal theta oscillations are travelling waves. *Nature* 459:534–539.
9. O'Keefe J, Recce ML (1993) Phase relationship between hippocampal place units and the EEG theta rhythm. *Hippocampus* 3:317–330.
10. Soltesz I, Deschênes M (1993) Low- and high-frequency membrane potential oscillations during theta activity in CA1 and CA3 pyramidal neurons of the rat hippocampus under ketamine-xylazine anesthesia. *J Neurophysiol* 70:97–116.
11. Maier N, et al. (2011) Coherent phasic excitation during hippocampal ripples. *Neuron* 72:137–152.
12. Colgin LL, et al. (2009) Frequency of gamma oscillations routes flow of information in the hippocampus. *Nature* 462:353–357.
13. Csicsvari J, Hirase H, Czurkó A, Mamiya A, Buzsáki G (1999) Fast network oscillations in the hippocampal CA1 region of the behaving rat. *J Neurosci* 19:RC20.
14. Sullivan D, et al. (2011) Relationships between hippocampal sharp waves, ripples, and fast gamma oscillation: Influence of dentate and entorhinal cortical activity. *J Neurosci* 31:8605–8616.
15. Girardeau G, Benchenane K, Wiener SI, Buzsáki G, Zugaro MB (2009) Selective suppression of hippocampal ripples impairs spatial memory. *Nat Neurosci* 12:1222–1223.
16. Jadhav SP, Kemere C, German PW, Frank LM (2012) Awake hippocampal sharp-wave ripples support spatial memory. *Science* 336:1454–1458.
17. Klausberger T, et al. (2003) Brain-state- and cell-type-specific firing of hippocampal interneurons in vivo. *Nature* 421:844–848.
18. Klausberger T, Somogyi P (2008) Neuronal diversity and temporal dynamics: The unity of hippocampal circuit operations. *Science* 321:53–57.
19. Royer S, et al. (2012) Control of timing, rate and bursts of hippocampal place cells by dendritic and somatic inhibition. *Nat Neurosci* 15:769–775.
20. Pinault D (1996) A novel single-cell staining procedure performed in vivo under electrophysiological control: Morpho-functional features of juxtacellularly labeled thalamic cells and other central neurons with biocytin or Neurobiotin. *J Neurosci Methods* 65:113–136.
21. Dombeck DA, Khabbaz AN, Collman F, Adelman TL, Tank DW (2007) Imaging large-scale neural activity with cellular resolution in awake, mobile mice. *Neuron* 56:43–57.
22. Harvey CD, Collman F, Dombeck DA, Tank DW (2009) Intracellular dynamics of hippocampal place cells during virtual navigation. *Nature* 461:941–946.
23. Baude A, et al. (1993) The metabotropic glutamate receptor (mGluR1 alpha) is concentrated at perisynaptic membrane of neuronal subpopulations as detected by immunogold reaction. *Neuron* 11:771–787.
24. Engel AK, Singer W (2001) Temporal binding and the neural correlates of sensory awareness. *Trends Cogn Sci* 5:16–25.
25. Womelsdorf T, et al. (2007) Modulation of neuronal interactions through neuronal synchronization. *Science* 316:1609–1612.
26. Sirota A, et al. (2008) Entrainment of neocortical neurons and gamma oscillations by the hippocampal theta rhythm. *Neuron* 60:683–697.
27. Atallah BV, Scanziani M (2009) Instantaneous modulation of gamma oscillation frequency by balancing excitation with inhibition. *Neuron* 62:566–577.
28. Buzsáki G, Wang XJ (2012) Mechanisms of gamma oscillations. *Annu Rev Neurosci* 35:203–225.
29. Senior TJ, Huxter JR, Allen K, O'Neill J, Csicsvari J (2008) Gamma oscillatory firing reveals distinct populations of pyramidal cells in the CA1 region of the hippocampus. *J Neurosci* 28:2274–2286.
30. Belluscio MA, Mizuseki K, Schmidt R, Kempter R, Buzsáki G (2012) Cross-frequency phase-phase coupling between θ and γ oscillations in the hippocampus. *J Neurosci* 32:423–435.
31. Ylinen A, et al. (1995) Sharp wave-associated high-frequency oscillation (200 Hz) in the intact hippocampus: Network and intracellular mechanisms. *J Neurosci* 15:30–46.
32. Csicsvari J, Hirase H, Mamiya A, Buzsáki G (2000) Ensemble patterns of hippocampal CA3-CA1 neurons during sharp wave-associated population events. *Neuron* 28:585–594.
33. Ellender TJ, Nissen W, Colgin LL, Mann EO, Paulsen O (2010) Priming of hippocampal population bursts by individual perisomatic-targeting interneurons. *J Neurosci* 30:5979–5991.
34. Armstrong C, Soltesz I (2012) Basket cell dichotomy in microcircuit function. *J Physiol* 590:683–694.
35. Bartos M, Elgueta C (2012) Functional characteristics of parvalbumin- and cholecystokinin-expressing basket cells. *J Physiol* 590:669–681.
36. Losonczy A, Zhang L, Shigemoto R, Somogyi P, Nusser Z (2002) Cell type dependence and variability in the short-term plasticity of EPSCs in identified mouse hippocampal interneurones. *J Physiol* 542:193–210.
37. Pouille F, Scanziani M (2004) Routing of spike series by dynamic circuits in the hippocampus. *Nature* 429:717–723.
38. Hefft S, Jonas P (2005) Asynchronous GABA release generates long-lasting inhibition at a hippocampal interneuron-principal neuron synapse. *Nat Neurosci* 8:1319–1328.

Varga et al.

www.manaraa.com

39. Földy C, Lee SY, Szabadics J, Neu A, Soltesz I (2007) Cell type-specific gating of perisomatic inhibition by cholecystokinin. *Nat Neurosci* 10:1128–1130.

40. Takács VT, Klausberger T, Somogyi P, Freund TF, Gulyás AI (2012) Extrinsic and local glutamatergic inputs of the rat hippocampal CA1 area differentially innervate pyramidal cells and interneurons. *Hippocampus* 22:1379–1391.

41. Kim J, et al. (2012) mGRASP enables mapping mammalian synaptic connectivity with light microscopy. *Nat Methods* 9:96–102.

42. Maccaferri G, McBain CJ (1996) The hyperpolarization-activated current (Ih) and its contribution to pacemaker activity in rat CA1 hippocampal stratum oriens-alveus interneurones. *J Physiol* 497:119–130.

43. Pike FG, et al. (2000) Distinct frequency preferences of different types of rat hippocampal neurones in response to oscillatory input currents. *J Physiol* 529: 205–213.

44. Gloveli T, et al. (2005) Differential involvement of oriens/pyramidale interneurones in hippocampal network oscillations in vitro. *J Physiol* 562:131–147.

45. Lawrence JJ, et al. (2006) Somatodendritic Kv7/KCNQ/M channels control interspike interval in hippocampal interneurons. *J Neurosci* 26:12325–12338.

46. Kispersky TJ, Fernandez FR, Economo MN, White JA (2012) Spike resonance properties in hippocampal O-LM cells are dependent on refractory dynamics. *J Neurosci* 32: 3637–3651.

47. Lovett-Barron M, et al. (2012) Regulation of neuronal input transformations by tunable dendritic inhibition. *Nat Neurosci* 15(3):423–430.

48. Tukker JJ, Fuentealba P, Hartwich K, Somogyi P, Klausberger T (2007) Cell type-specific tuning of hippocampal interneuron firing during gamma oscillations in vivo. *J Neurosci* 27:8184–8189.

49. Reyes A, et al. (1998) Target-cell-specific facilitation and depression in neocortical circuits. *Nat Neurosci* 1:279–285.

50. Otte S, Hasenstaub A, Callaway EM (2010) Cell type-specific control of neuronal responsiveness by gamma-band oscillatory inhibition. *J Neurosci* 30:2150–2159.

51. Hu H, Martina M, Jonas P (2010) Dendritic mechanisms underlying rapid synaptic activation of fast-spiking hippocampal interneurons. *Science* 327:52–58.

52. Nörenberg A, Hu H, Vida I, Bartos M, Jonas P (2010) Distinct nonuniform cable properties optimize rapid and efficient activation of fast-spiking GABAergic interneurons. *Proc Natl Acad Sci USA* 107:894–899.

53. Martina M, Vida I, Jonas P (2000) Distal initiation and active propagation of action potentials in interneuron dendrites. *Science* 287:295–300.

54. Bartos M, et al. (2002) Fast synaptic inhibition promotes synchronized gamma oscillations in hippocampal interneuron networks. *Proc Natl Acad Sci USA* 99: 13222–13227.

55. Bartos M, Vida I, Jonas P (2007) Synaptic mechanisms of synchronized gamma oscillations in inhibitory interneuron networks. *Nat Rev Neurosci* 8:45–56.

56. Wulff P, et al. (2009) Hippocampal theta rhythm and its coupling with gamma oscillations require fast inhibition onto parvalbumin-positive interneurons. *Proc Natl Acad Sci USA* 106:3561–3566.

57. Gentet LJ, et al. (2012) Unique functional properties of somatostatin-expressing GABAergic neurons in mouse barrel cortex. *Nat Neurosci* 15:607–612.

58. Chrobak JJ, Buzsáki G (1998) Gamma oscillations in the entorhinal cortex of the freely behaving rat. *J Neurosci* 18:388–398.

59. Niell CM, Stryker MP (2010) Modulation of visual responses by behavioral state in mouse visual cortex. *Neuron* 65:472–479.

60. Zar JH (1999) *Biostatistical Analysis* (Prentice Hall, Upper Saddle River, NJ).

61. Kanji GK (1999) *100 Statistical Tests* (SAGE, London).

62. Bienvenu TC, Busti D, Magill PJ, Ferraguti F, Capogna M (2012) Cell-type-specific recruitment of amygdala interneurons to hippocampal theta rhythm and noxious stimuli in vivo. *Neuron* 74:1059–1074.

63. Berens P (2009) CircStat: A circular statistics toolbox for Matlab. *J Stat Softw* 31:1–21.